Enhanced Resistance to the Atomic Oxygen Exposure of POSS/Polyimide Composite Fibers with Surface Enrichment through Wet Spinning

Fangfang Liu,[a,b](刘芳芳) Haiquan Guo,[a]（郭海泉） Yong Zhao,[a]（赵勇）Xuepeng Qiu,*,[a]（邱雪鹏）Lianxun Gao,*,[a]（高连勋）

[a]Polymer Composites Engineering Laboratory, Changchun Institute of Applied Chemistry, Chinese Academy of Sciences, Changchun 130022, China（中国科学院长春应用化学研究所，高分子复合材料工程实验室）,[b]University of Chinese Academy of Sciences, Beijing 100049, China（中国科学院大学）*

Correspondence to: Xuepeng Qiu E-mail: *xp_q@ciac.ac.cn*

ABSTRACT: We report a series of PI composite fibers containing polyhedral oligomeric silsesquioxane (POSS). These fibers were fabricated by a three-step process consisting of the in situ polycondensation of POSS and polyamic acid, wet spinning, and thermal imidization. X-ray photoelectron spectroscopy (XPS) and energy-dispersive X-ray spectroscopy proved that POSS enriched the surface of POSS/PI composite fibers during wet spinning. This surface enrichment enhanced the resistance to atomic oxygen (AO) erosion. After exposing the POSS/PI composite fibers to AO fluence up to 2.93×10^{20} atoms cm^{-2}, the fibers still displayed excellent AO resistance. With increased POSS content from 0 wt% to 20 wt%, the retention of fracture strength and initial modulus considerably improved from 54% to 93% and from 64% to 91%, respectively. Moreover, the decay rates of fracture strength of the composite fibers obviously decreased at the same AO fluence with increased POSS content from 0 wt% to 20 wt%. AO erosion at a larger fluence further resulted in more effective AO resistance for composite fibers with higher POSS content. XPS results suggested as well that silicate passivated layers formed on the fiber surfaces after AO exposure, and these layers prevented the fibers from further AO erosion.

KEYWORDS: polyimide fibers, polyhedral oligomeric silsesquioxane, atomic oxygen, surface enrichment

1. INTRODUCTION

Polymeric fibers and fabrics have been applied extensively to the flexible construction elements of spacecraft mounted on their external surfaces. Such elements include different fastener assemblies, tensional cables, flexible sheetings and screens, railings, and safety lines used by astronauts [1,2]. These polymeric fibers are subjected to high-energy atomic oxygen (AO) attack (~4.5 eV) in low Earth orbit (LEO), which is the dominant composition of the upper atmosphere of Earth in the altitude between 200 and 700 km [3]. Such attack causes the rapid degradation of polymer materials and leads to hazards on the mechanical properties [4-9]. The resistance of polymeric fibers to AO attack can be improved by utilizing AO-durable coatings, such as SiO_2, Al_2O_3, or SnO_2 [10-13]. However, these inorganic coating materials are prone to crack and even peel off from the fiber surface during thermal cycling, folding, or bending because of the insufficient adhesive strength and the difference in thermal expansion coefficients between the inorganic coatings and polymeric fibers [14]. The cracks in the coating allow AO to attack the underlying polymeric fibers and can result in undercutting phenomena, and ultimately, mechanical failure of the polymeric fibers.

A promising approach for producing LEO survivable polymeric fibers is incorporating oxidation-resistant nanoscale components in the form of additives into the polymer matrix. Polyhedral oligomeric silsesquioxane (POSS, empirical formula $RSiO_{1.5}$) are ideal candidates for this approach [15-19]. POSS-containing polymer nanocomposites have shown significantly lower AO erosion yields versus pure polymer. In Minton's study [16], POSS was incorporated into the main chain and side chain of polyimide (PI) backbone to produce two types of POSS/PI. After AO erosion, these two types showed similar resistance performances. Depending on the weight percentage of the POSS cage, the erosion yield of the POSS/PI may

be as low as ~0.01 that of the pure PI (or Kapton H). With a hyperthermal AO fluence of 2.70 $\times 10^{20}$ atoms cm^{-2}, the erosion yields of 7.0 wt% Si_8O_{12} side chain POSS/PI and 7.0 wt% Si_8O_{11} main chain POSS/PI were 0.15 and 0.13×10^{-24} cm^3 $atom^{-1}$, respectively. According to Lei's report [20], POSS modified by two amine was copolymerized with 4,4′-oxydianiline (ODA) and pyromellitic dianhydride (PMDA) to prepare POSS/PI. The composites containing 29.7 wt% POSS showed the lowest erosion yield of 0.9×10^{-25} cm^3 $atom^{-1}$. The as-prepared POSS/PI copolymers not only manifested excellent AO resistance but also displayed good thermal and mechanical properties. Nevertheless, the preparation process was complicated, difficult to operate, and relatively costly. In this regard, Qian [17] *et al.* prepared several trisilanolphenyl POSS/PI blends with different contents of POSS, and the AO resistance of the blends and POSS/PI copolymers was further investigated. For all POSS/PI materials, the AO resistance increased with increased POSS cage loading, which became more effective at higher AO fluence. Under similar POSS cage loadings and exposure conditions, the TSP POSS/PI blends showed comparable erosion yields to the POSS/PI copolymers, with specific samples of blends and copolymers achieving erosion yields as low as 0.066×10^{-24} cm^3 $atom^{-1}$ with an AO fluence of 5.93×10^{20} atoms cm^{-2}.

A major challenge in the development of polymer nanocomposites is the control of nanoparticle dispersion in polymer matrix [21,22]. However, these studies essentially focused on the efficient and homogenous dispersion of nanoparticles within a whole matrix and the suppression of aggregation of a nanoparticulate phase; scarce literature reported on utilizing enrichment in polymer/nanoparticle nanocomposites to create surfaces with specific morphologies [23,24]. Certain applications can benefit from the targeted arrangement of nanoparticles on polymer surfaces [25]. The ideal situation for the resistance to AO erosion involves the nanoparticles being confined to the polymer surface.

Surface enrichment in melt-blended POSS/polymer nanocomposites has been reported [26]. Researchers demonstrated that the surface enrichment of POSS nanoparticles helps improve the surface hydrophobicity and tribological properties of POSS/polymer nanocomposites by annealing the melt and heating the solid blend [27]. POSS nanoparticles show preferential enrichment to air–polymer interfaces, which are driven by low surface energy, and the formation of larger aggregates at the surface than in the bulk [28,29]. However, the majority of these studies to date have focused on polymer bulk and film materials [30]. Only few works centered on nanoparticle dispersion and morphological evolution in polymer fibers during wet spinning, which is commonly utilized in high-performance fiber manufacturing for materials such as aramid, poly(p-phenylenebenzobisoxazole), carbon, and PI fibers. In wet spinning, the dual diffusion of the solvent and nonsolvent between the fresh fluid filament and the coagulation bath cause the polymer solidification, which is the fundamental process governing the fiber structure [31,32]. The migration of POSS in nanocomposites may be driven by the counter diffusion of solvent and nonsolvent, which are totally different from the surface enrichment of the POSS in melt-blended POSS/polymer nanocomposites.

Aromatic PI fibers are desirable spacecraft materials because of their excellent thermal stability, chemical resistance, and outstanding mechanical properties [33-38]. However, PI fibers are eroded significantly under AO exposure [39]. In our previous work, AO-resistant properties of PI fibers containing phosphorous groups in PI molecular chains have been reported [40-43]. With increased phosphorus content of PI fibers from 0% to 60%, mass loss of the fibers decreased significantly from 1.80 mg cm^{-2} to 0.75 mg cm^{-2}, the retention of tensile strength and Young's modulus of the fibers significantly increased from 47.78% to 64.87% and from 59.15% to 66.04% under the highest AO fluence of 5.0×10^{20} atoms cm^{-2}.

In this study, a series of novel POSS/PI composite fibers was fabricated by a three-step process consisting of the in situ polycondensation of POSS and polyamic acid (PAA), wet spinning, and then thermal imidization. The dispersion behavior of POSS in composite fiber was systematically investigated. The current investigation will provide some suggestion on controlling the surface enrichment of POSS during wet spinning and improving the resistance to AO erosion.

2. EXPERIMENTAL METHODS

2.1. Materials

ODA (>99.5%) and PMDA were purchased from Shanghai Research Institute of Synthetic Resins, and PMDA was dried in vacuum at 233 °C for 2 h prior to use. *N*,*N*-Dimethylacetamide (DMAc, analytical purity ≥99.5%) was purchased from Tianjin Fine Chemical Co., Ltd. and distilled over CaH_2 under reduced pressure. Trisilanolphenyl POSS was obtained from Hybrid Plastics, Inc. Kapton® H films were purchased from DuPont, Inc. All other chemicals were used as received.

2.2. Preparation of POSS/PAA Solutions

The preparative route of POSS/PI fibers by wet spinning is shown in Scheme 1. A series of POSS/PAA solutions was initially prepared from mixtures of ODA, PMDA, and different POSS contents. The POSS/PAA solutions with 10 wt% POSS was prepared as follows. POSS (13.20 g, 0.01 mol) and ODA (56.80 g, 0.28 mol) were charged into a flask equipped with a stirrer under nitrogen atmosphere, followed by the addition of DMAc (672.0 g). The solution was stirred for 1 h, and then PMDA (61.87 g, 0.28 mol) was added under stirring at 0 °C. The resulting solution was stirred for another 24 h at room temperature. Other POSS/PAA solutions containing 5 wt%, 15 wt%, and 20 wt% of POSS were also prepared through the same steps.

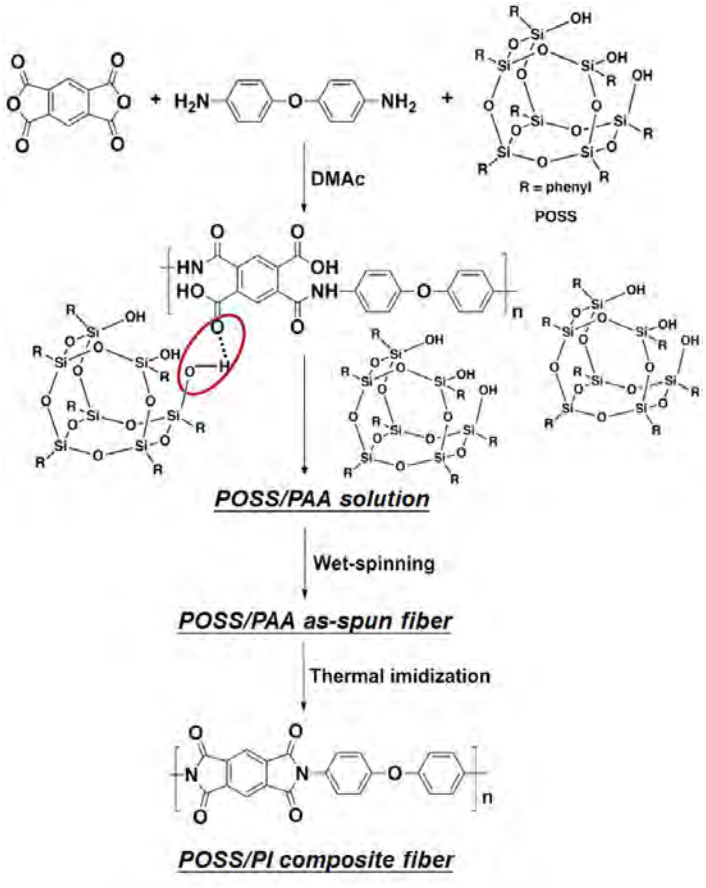

Scheme 1. Synthetic route of POSS/PI composite fibers.

2.3. Preparation of POSS/PI Composite Fibers

The POSS/PI composite fibers were spun by wet spinning with a homemade spinning machine as shown in Scheme 2 [44]. The viscous POSS/PAA solutions in DMAc were filtered, degassed, and then extruded through a spinneret (100 holes, 0.12 mm/hole) at room temperature. The fresh fluid filaments were entered into a coagulation bath (mixture of water and DMAc with a volume ratio of 1:1) and coagulated into

nascent fibers, followed by washing thoroughly with water and drying to remove residual solvent. The as-spun POSS/PAA fibers were subjected to thermal imidization at 350 °C followed by heat drawing with the ratio of 1.5 at 480 °C to produce POSS/PI composite fibers. The diameters of all the fibers were in the range of 15-20 μm.

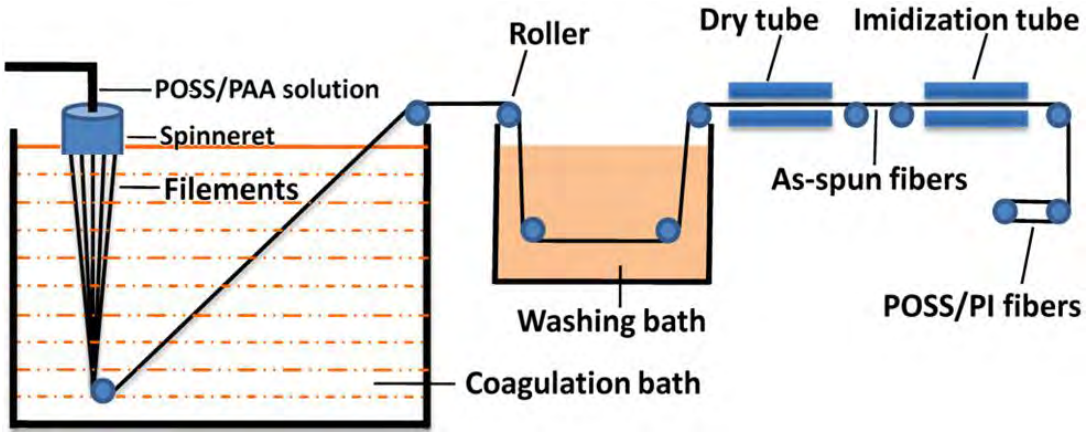

Scheme 2. Schematic of the wet spinning of POSS/PI composite fibers.

2.4. Morphological, Structural, and Chemical Composition Characterization

Fourier transform infrared (FTIR) spectrum was recorded on a VERTEX 70 spectrometer at a spectral resolution of 400-4000 cm^{-1}. The surface chemical composition of fibers before and after AO exposure was analyzed by XPS using an ESCALAB 250Xi electron spectrometer from Thermo Scientific Corporation with monochromatic Al Kα radiations. The morphology of surface and cross-section of fibers before and after AO exposure were examined by a field-emission scanning electron microscopy (SEM, Hitachi S-4800). The samples were sprayed with Pt before observation. The chemical composition of fiber cross-section was investigated using energy dispersive X-ray spectroscopy (EDX, Bruker) in conjunction with SEM to determine their Si, O, and C contents. To observe the POSS-rich domains, the elemental mapping of these sections were also analyzed on the sample images.

2.5. Thermal and Mechanical Characterization

Dynamic mechanical analysis (DMA) was conducted by a Rheometric Scientific DMTA-V at 1 Hz with the heating rate of 3 °C min^{-1} in a temperature range from 100 °C to 450 °C. Thermogravimetric analysis (TGA) was then performed with a TA Q50 instrument at a heating rate of 10 °C min^{-1} from 50 °C to 800 °C under nitrogen atmosphere. The measurement of mechanical properties was carried out on an XQ-1 instrument at a strain rate of 20 mm min^{-1}, and the initial distance between grippers was 20 mm. Each sample was tested more than 20 times, and the average value was used for the final properties.

2.6. Ground-based Simulated AO Exposure Experiment

The AO exposure experiment was performed in a ground-based AO effects simulation facility, a type of filament discharging plasma-type atomic oxygen simulation facility. Collision ionization and the dissociation of oxygen molecules by electrons formed oxygen plasma, which mainly includes neutral O atoms, electrons, O_2^+, O^+, and molecular oxygen. PI fibers of 20 cm length were placed on the platform in a vacuum chamber for AO exposure. In this work, different AO irradiation times were used (Table 1). The corresponding AO fluence of each irradiation test was calculated on the basis of the mass loss, irradiated area, density, and erosion yield of the Kapton® H film as described by the literatures [1, 44, 45]. The Kapton films were cut into 1×1 cm^2 squares and placed on the platform randomly for the average AO fluence. All the samples were weighed at 5, 10, 15, 20, and 30 h. AO fluence was calculated from the mass loss of Kapton® H film through Equation (1):

$$F = \Delta M / (\rho A E) \qquad (1)$$

where F is the total AO fluence (atoms cm^{-2}), ΔM was the mass loss of Kapton (g), ρ was the density of Kapton (1.42 g cm^{-3}). A was the exposure area of Kapton (1 cm^2), and E was the erosion constant of Kapton (3×10^{-24} cm^3 $atom^{-1}$). The AO stream in the vacuum chamber was nearly uniform in our experiment. The POSS/PI composite film and POSS/PI composite fiber samples were weighed and analyzed after different AO exposure times [46].

Table 1. Experimental conditions of the simulated AO exposure.

AO exposure time (h)	5	10	15	20	30
AO fluence (atoms cm^{-2})	5.40×10^{19}	1.01×10^{20}	1.48×10^{20}	1.94×10^{20}	2.93×10^{20}

3. RESULTS AND DISCUSSION

3.1. Structural Characterization of POSS/PI Composite Fibers

Fig. 1 shows the FTIR spectra of POSS nanoparticles, PI fiber, and POSS/PI composite fibers with different POSS loading. For the PI fiber, the peaks at 1774 and 1722 cm^{-1} belong to the C=O group of asymmetric and symmetric stretching vibrations of the aromatic imide ring, respectively. The peak at 1360 cm^{-1} is attributed to the C–N stretching vibration of the imide ring. The peak at 734 cm^{-1} implies the appearance of imide ring bending vibration. The above-mentioned results indicate that PAA fibers have been successfully converted into PI fibers. For POSS/PI composite fibers, new bands are obviously detected. The two peaks at 1428 and 690 cm^{-1} are attributed to the Ar–Si and Si–C stretching vibrations, respectively, of POSS. Moreover, with increased POSS content from 0% to 20%, the intensity of the two peaks above showed a clear increase, which indicates that the POSS is introduced into the PI fibers successfully.

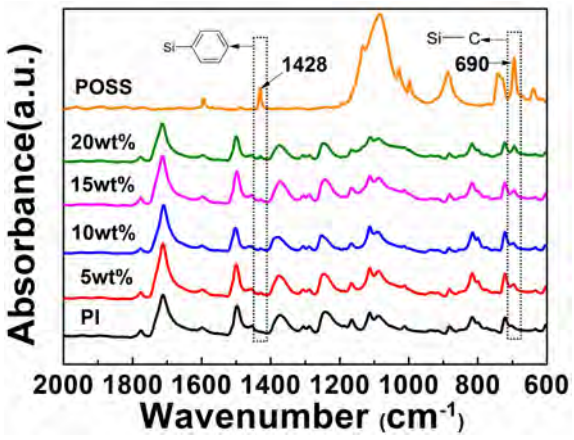

Fig. 1. FTIR spectra of POSS nanoparticles, PI fiber, and POSS/PI composite fibers with the POSS content of 5 wt%, 10 wt%, 15 wt%, and 20 wt%.

1. 3.2. Distribution of POSS in the Composite Fibers

To evaluate the POSS content on the surface of POSS/PI composite fibers, the quantitative analysis of the surface elemental composition is initially carried out by XPS based on the silicon percentage on the surface, and the corresponding results are listed in Table 2. With increased POSS addition from 5 wt% to 20 wt%, the silicon content on fiber surface shows an obvious increase from 6.52 wt% to 10.58 wt%. On the basis of POSS addition content, the calculated silicon content in composite fibers were 2.42 wt%, 4.50 wt%, 6.35 wt%, and 7.99 wt%, corresponding to POSS addition of 5 wt%, 10 wt%, 15 wt%, and 20 wt%, respectively. Obviously, both experimental and calculated values of silicon content in composite fibers showed an increase with increased POSS addition amount. However, the experimental values of silicon

content on the fiber surface were higher than the calculated silicon content in composite fibers. The results indicate the enrichment of POSS nanoparticles on the surface of composite fibers through wet spinning. To confirm these findings, we used energy dispersive X-ray in a scanning electron microscope (SEM-EDX) and EDX Si mapping to further study the distribution of POSS in composite fibers by observing the cross-sectional morphologies of samples prepared by brittle breaking at low temperature. The POSS contents of the specific locations, i.e., near surface and center in the cross-sectional area of composite fibers, were determined, and the Si contents were fairly variable along the radial direction of the fiber cross-section (Fig. 2). Additional silica content was clearly observed near the fiber surface than at the fiber center. Moreover, the low POSS amount added in fibers gave rise to the obvious distributed disparity (Fig.s a2-a3, b2-b3, and c2-c3) corresponding to the fibers with POSS contents of 5 wt%, 10 wt% and 15 wt%. When the POSS addition amount was increased to 20 wt%, the small difference in silicon distribution is shown in Fig.s d2-d3. We also performed a quantitative analysis on silica content by SEM-EDX, and the results are listed in Table 2. When the added POSS amount was raised from 5 wt% to 20 wt%, the silicon contents near the fiber surface showed a clear increase from 5.81 wt% to 11.58 wt%, and those in the fiber center displayed an increase from 1.22 wt% to 3.28 wt%. Specifically, the silicon contents near the fiber surface were 5.81 wt%, 8.29 wt%, 10.25 wt% and 11.58 wt%, and those in the fiber center were 1.22 wt%, 2.46 wt%, 2.83 wt%, and 3.28 wt%, corresponding to the added POSS amount of 5 wt%, 10 wt%, 15 wt% and 20 wt%. Notably, the calculated silicon contents in the fiber bulk were much lower than the contents near the fiber surface, but higher than the contents in the fiber center. The results confirmed the POSS enrichment on the surface of the POSS/PI composite fibers.

Table 2. Calculated and measured values of silicon content in the POSS/PI composite fibers.

Sample	POSS (wt%)	Calculated silicon[a] (wt%)	Near-surface		
			Surface [b] (wt%)	[c] (wt%)	Center [c] (wt%)
5 wt% POSS/PI	5.0	2.42	6.52	5.81	1.22
10 wt% POSS/PI	10.0	4.50	8.00	8.29	2.46
15 wt% POSS/PI	15.0	6.35	9.82	10.25	2.83
20 wt% POSS/PI	20.0	7.99	10.58	11.58	3.28

[a]The theoretical value calculated by the addition of POSS
[b]The surface silicon content by XPS.
[c]The silicon content from cross-section by EDX.

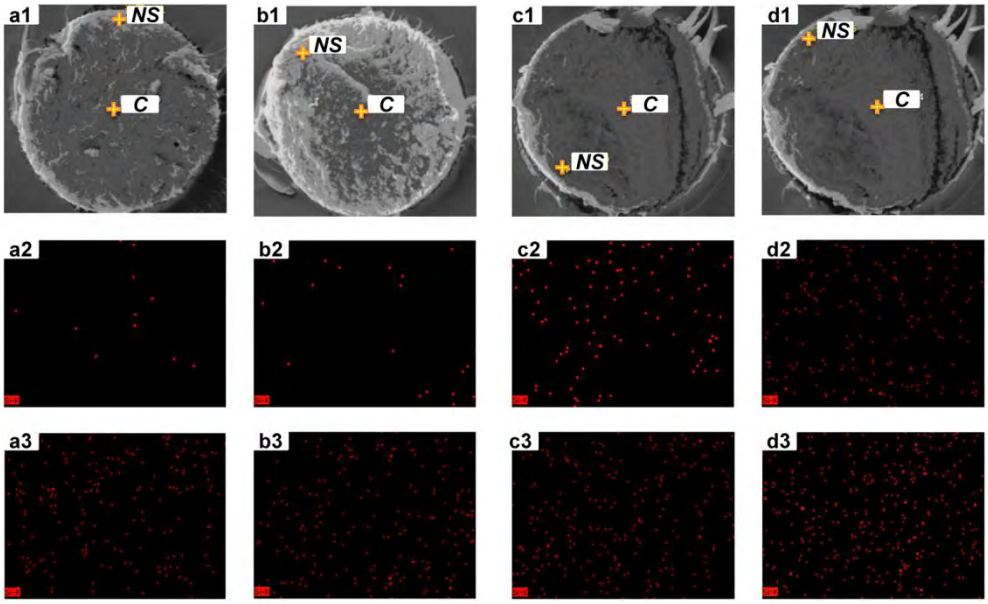

Fig. 2. Si elemental analysis of the cross-section of 5 wt% POSS/PI (a1-a3), 10 wt% POSS/PI (b1-b3), 15 wt% POSS/PI (c1-c3), and 20 wt% POSS/PI (d1-d3) by the SEM-EDX. *C* means the scanning areas at the fiber central cross-section, and *NS* represents the scanning areas near the fiber surface. a2-d2 show the Si mapping at the central region (*C*), and a3-d3 display the Si mapping near the surface region (*NS*).

The formation of surface enrichment is mainly ascribed to the double diffusion process of the solvent and the nonsolvent during fiber coagulation (Scheme 3). In wet spinning, when the viscous solution of POSS/PAA in DMAc is extruded through small holes of a spinneret and enters into the coagulation bath (DMAc/water), the solvent (DMAc) molecules begin to diffuse out of the freshly formed fluid filament, and non-solvent (water) molecules diffuse in simultaneously [47]. This process is the primary mechanism for the polymer solidification into fibers from solution in the coagulation bath, which is a quaternary system consisting of the polymer, solvent, nonsolvent, and nanoparticle. The main factors affecting the surface enrichment of fibers during the coagulation process include concentrations of DMAc, H_2O and POSS, radius of the extruded filaments, thickness of the outer layer gel phase, and spinning speed. Scheme 3 shows a sectional view of a single extruded filament. The *Z* axis is the axial direction beginning from the spinneret to the take-up roller along the bath. The *R* axis is the radial direction on the fiber starting from the center to the outer surface. The dual diffusion initially occurs on the surface of the fluid filament, and a layer of skin forms. The thin skin disrupts the dual diffusion process and restrains the POSS diffusion out of the fibers. The different diffusion rates of DMAc and H_2O from the solidified filament is a dominant factor affecting the POSS diffusion in the coagulation process. With the outward diffusion of DMAc, POSS nanoparticles show favorable mobility and diffuse from the center to the surface of the filaments, attributing to better miscibility of POSS (solubility parameter of 9.8×10^{-3} (cal $m^{-3})^{1/2}$) and DMAc (solubility parameter of 11.1×10^{-3} (cal $m^{-3})^{1/2}$) than that of POSS and water (solubility parameter of 23.2×10^{-3} (cal $m^{-3})^{1/2}$) [48]. A kinetic competition between POSS outward diffusion and the gradual thickening of the outer layer gel phase impacts the dispersion characteristic of POSS, which results in the formation of surface enrichment of POSS in composite fibers. The preferential migration of POSS offers an avenue to surface modification.

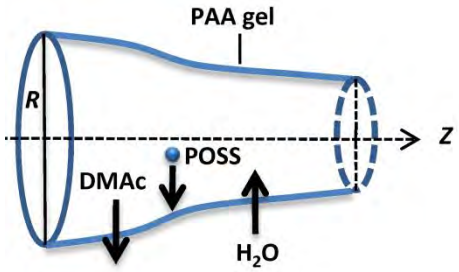

Scheme 3. Schematic of extruded PAA filament in the coagulation bath and the dual diffusion process.

3.3. Thermal Properties of POSS/PI Composite Fibers.

The glass-transition temperatures (T_g) of the fibers are investigated by DMA. As shown in Table 3 and Fig. 3a, the T_g of composite fibers increases from 382 °C to 401 °C with increased POSS content from 0 wt% to 20 wt%. The results indicate that incorporating POSS can confine the segmental motion of the PI chain because of the π–π stacking of the phenyl rings in PI and the hydrogen bond interactions between the trisilanolphenyl groups in POSS and carbonyl groups [49].

Fig. 3b shows the TGA curves of the PI and composite fibers. With increased POSS content from 5 wt% to 20 wt%, the 5% weight-loss temperatures ($T_{5\%}$) of the composite fibers are in the range of 560–570 °C, which indicates excellent thermal stability similar to that of PI fibers with the $T_{5\%}$ value of 568 °C (Table 3).

Table 3. Thermal and mechanical properties of POSS/PI composite fibers.

Sample	Thermal Properties		Mechanical Properties		
	T_g (°C)	$T_{5\%}$ (°C)	Fracture strength (GPa)	Initial modulus (GPa)	Elongation (%)
PI	382	568	0.58 ± 0.03	7.41 ± 0.33	8.01 ± 0.77
5 wt% POSS/PI	390	568	0.59 ± 0.02	7.37 ± 0.40	8.27 ± 0.43
10 wt% POSS/PI	397	570	0.60 ± 0.04	7.58 ± 0.41	9.08 ± 0.74
15 wt% POSS/PI	400	564	0.56 ± 0.03	7.22 ± 0.39	8.59 ± 0.66
20 wt% POSS/PI	401	560	0.44 ± 0.03	6.78 ± 0.46	7.95 ± 0.50

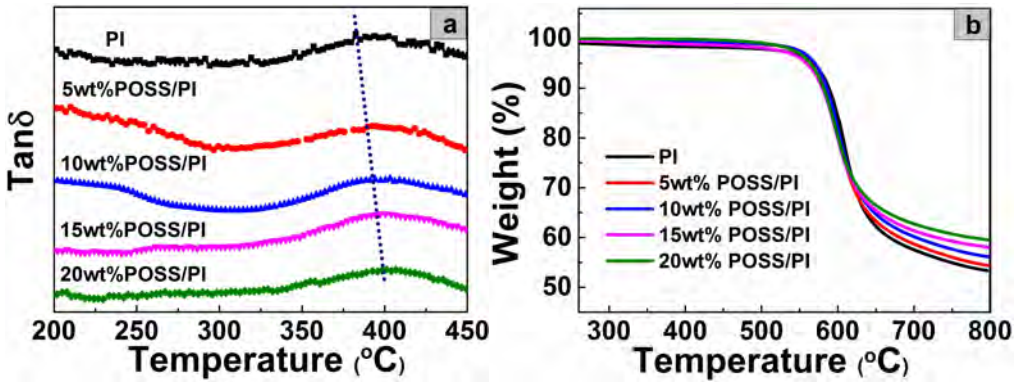

Fig. 3. DMA and TGA curves of PI and POSS/PI fibers.

3.4. Mechanical Properties of POSS/PI Composite Fibers

For the requirements of space application, the mechanical property is considered a significant parameter [26]. Fig. 4 shows the variation of mechanical properties with different POSS contents. With increased POSS content from 0 wt% to 10 wt%, the mechanical properties of POSS/PI composite fibers only display a negligible increase in fracture strength and initial modulus with the average values of 0.59 GPa and 7.48 GPa compared with the pristine PI fiber with a fracture strength of 0.58 GPa and initial modulus of 7.41 GPa. When the POSS content was increased to 15%, the mechanical properties of the fibers deteriorated, and the fracture strength and initial modulus became 0.56 GPa and 7.22 GPa, respectively. However, when the POSS loading reached 20 wt%, the fracture strength and initial modulus of the fibers decreased to 0.44 GPa and 6.78 GPa, respectively. Although the interactions of hydrogen bonds and π–π stacking exist in a composite fiber system, surface enrichments cause the aggregation of POSS nanoparticles on the fiber surface, which can weaken the above interactions. Moreover, when amount of POSS added exceeds a certain critical value, POSS nanoparticles aggregate on the surface and in the bulk and produce defect points in the PI matrix. These observations show the negative effects on the mechanical properties of POSS/PI composite fibers.

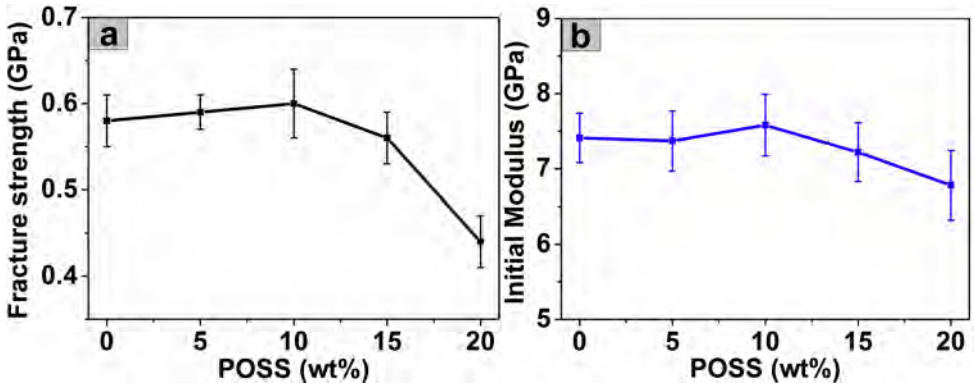

Fig. 4. Fracture strength (a) and initial modulus (b) of POSS/PI composite fibers added with different POSS amounts.

3.5. Mass Loss and Surface Morphologies of Fibers after AO Erosion

The POSS/PI composite fibers are exposed to variable simulated AO fluences between 5.4×10^{19} atoms cm^{-2} and 2.93×10^{20} atoms cm^{-2} to characterize their resistance to an AO environment.

In the current work, the mass loss of POSS/PI composite films was replaced by those of corresponding fibers. As a result, the low weights of the fibers lead to error in the mass test. The mass loss in the films is shown in Table 4 and Fig. 5. In the whole test, the Kapton® film is used as a standard. With increased AO fluence from 5.4×10^{19} atoms cm^{-2} to 2.93×10^{20} atoms cm^{-2}, the mass loss of Kapton film and pristine PI film showed a clear increase from 0.023 mg cm^{-2} to 0.125 mg cm^{-2} and 0.025 mg cm^{-2} to 0.110 mg cm^{-2}. For the POSS/PI films, the mass loss revealed a lower decrease than that of the mass losses of Kapton and pristine PI film. With the increase of AO from 5.4×10^{19} atoms cm^{-2} to 2.93×10^{20} atoms cm^{-2}, the mass losses of 5 wt% POSS/PI, 10 wt% POSS/PI, 15 wt% POSS/PI, and 20 wt% POSS/PI exhibited slow increases from 0.01 mg cm^{-2} to 0.04 mg cm^{-2}, 0.005 mg cm^{-2} to 0.035 mg cm^{-2}, 0.005 mg cm^{-2} to 0.020 mg cm^{-2}, 0.005 mg cm^{-2} to 0.015 mg cm^{-2}, respectively. Under the same AO fluence, the mass loss of the POSS/PI films decreased with a rise in POSS content. With increased POSS content from 0 wt% to 20 wt%, the mass loss of the films decreased from 0.025 mg cm^{-2} to 0.005 mg cm^{-2} at 5.40×10^{19} mg cm^{-2} AO fluence, from 0.04 mg cm^{-2} to 0.005 mg cm^{-2} at 1.01×10^{20} atoms cm^{-2} AO fluence, from 0.06 mg cm^{-2} to 0.01 mg cm^{-2} at 1.48×10^{20} atoms cm^{-2} AO fluence, from 0.075 mg cm^{-2} to 0.01 mg cm^{-2} at 1.94×10^{20} atoms cm^{-2} AO fluence, and from 0.11 mg cm^{-2} to 0.015 mg cm^{-2} at 2.93×10^{20} atoms cm^{-2} AO fluence. Notably, when the POSS contents were raised to 15 wt% and 20 wt%, the mass loss showed the same values at low AO fluence, i.e., 5.40×10^{19} atoms cm^{-2}, 1.01×10^{20} atoms cm^{-2}, 1.48×10^{20} atoms cm^{-2}, and 1.94×10^{20} atoms cm^{-2} AO fluence. Results indicated that the AO resistance of the POSS/PI films improved with augmenting POSS content. With

increased POSS content to a certain extent, i.e., 20 wt%, the AO resistance seems to be a constant at low AO fluence.

Table 4. Mass loss of PI films under different AO fluences.

Sample	Mass loss[a]				
	5.40×10^{19} atoms cm^{-2} (mg cm^{-2})	1.01×10^{20} atoms cm^{-2} (mg cm^{-2})	1.48×10^{20} atoms cm^{-2} (mg cm^{-2})	1.94×10^{20} atoms cm^{-2} (mg cm^{-2})	2.93×10^{20} atoms cm^{-2} (mg cm^{-2})
Kapton film	0.023	0.043	0.063	0.083	0.125
Pristine PI	0.025	0.040	0.060	0.075	0.110
5 wt% POSS/PI	0.010	0.020	0.025	0.030	0.040
10 wt% POSS/PI	0.005	0.010	0.020	0.025	0.035
15 wt% POSS/PI	0.005	0.005	0.010	0.010	0.020
20 wt% POSS/PI	0.005	0.005	0.010	0.010	0.015

[a] Using Equation (1) to calculate the total AO fluence with Kapton® film in this Table.

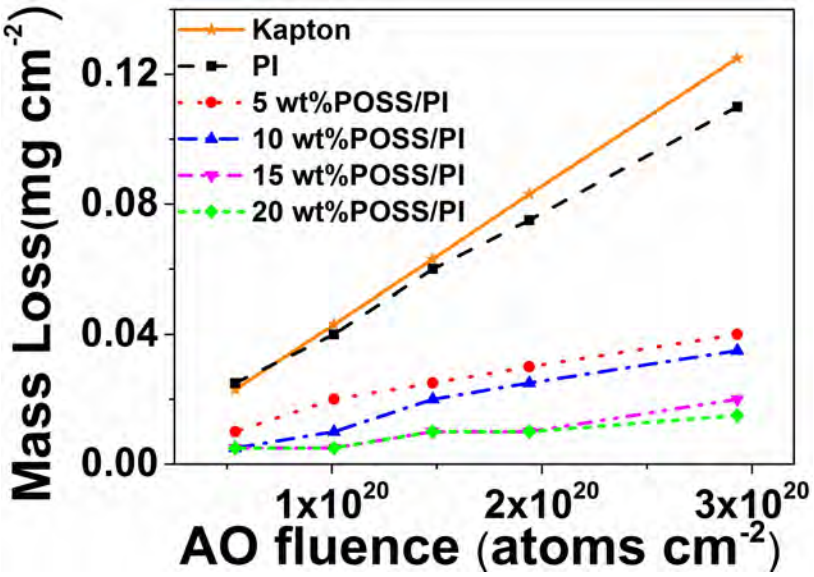

Fig. 5. Mass loss of POSS/PI films versus AO fluence.

SEM observation provides a visualized understanding on the surface morphological evolution in Fig. 6. Prior to the AO exposure, the surfaces of all fibers were smooth and flat without obvious defects (Fig.s 6a0-e0). After AO exposure experiment with increased fluence from 0 atoms cm^{-2} to 2.93×10^{20} atoms cm^{-2}, the surface morphologies of all fibers changed distinctly from smooth to gully like and displayed numerous densely distributed etching tunnels. For pristine PI fibers, the numbers and sizes of etching tunnels dramatically increased, and the "gully-like" morphology broadened and deepened with increased AO fluence from 1.01×10^{20} atoms cm^{-2} to 2.93×10^{20} atoms cm^{-2} (Fig. 6(a1-a3)). This effect resulted in the coalescence of rims and formation of interconnected net structure. Obviously, the pristine PI fiber suffers serious AO

surface erosion under the given AO fluence. This kind of "gully-like" morphology may be due to the "undercutting" effects of AO erosion. The high-energy AO impacted the fiber surface and formed the defect points (pits or cracks) and served as channels for the AO to undercut into the polymer. All the defect points were amplified with the extension in AO erosion time [50]. However, the surface morphologies of POSS/PI composite fibers showed obvious improvement compared with that of the pristine PI fiber after the AO exposure experiment. With increased POSS content from 5 wt% to 15 wt%, the surface roughness of composite fibers showed a clear decrease after exposure at the same AO fluence, although the roughness of the fibers displayed increased AO fluence from 0 atom cm^{-2} to 2.93×10^{20} atoms cm^{-2}. Notably, when the added POSS content reached 20 wt%, the surface roughness of composite fibers showed a slight change without obvious defect, even when the AO fluence was increased to 2.93×10^{20} atoms cm^{-2} (Fig. 6(e3)). Actually, the POSS cage was further oxidized to silica, and a self-passivating network was created on the surface of POSS/PI composite fibers under AO exposure; this network can then protect the fibers from further AO erosion [19].

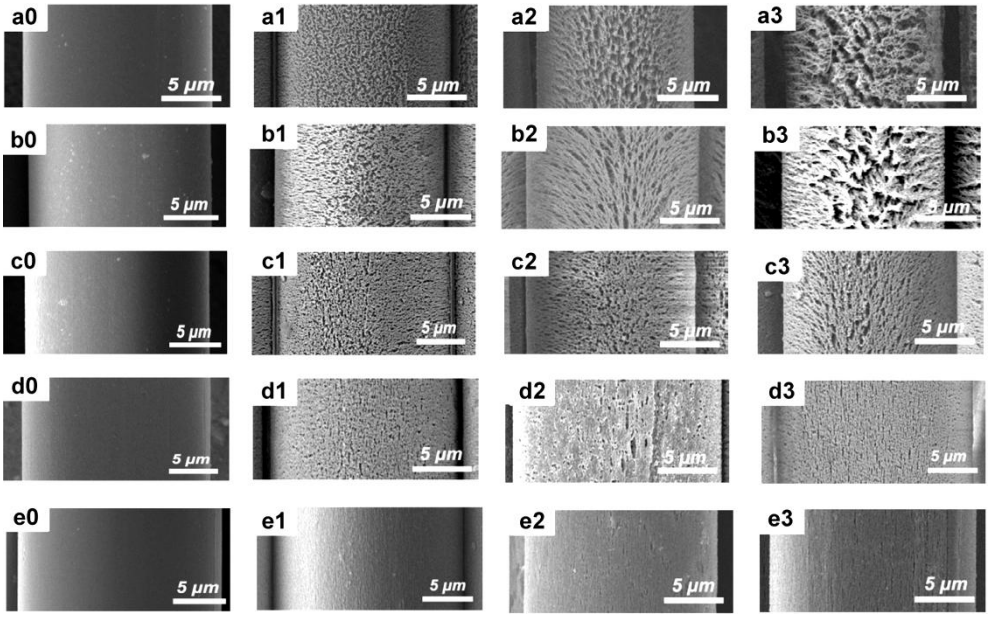

Fig. 6. Fiber surface morphologies of (a0-a3) pure PI, (b0-b3) 5 wt% POSS/PI, (c0-c3) 10 wt% POSS/PI, (d0-d3) 15 wt% POSS/PI, and (e0-e3) 20 wt% POSS/PI after exposure to AO with a fluence at (a0-e0) 0, (a1-e1) 1.01×10^{20} atoms cm^{-2}, (a2-e2) 1.94×10^{20} atoms cm^{-2}, and (a3-e3) 2.93×10^{20} atoms cm^{-2}.

3.6. Surface Elemental Analysis by XPS after AO Erosion

To reveal the AO resistance mechanism of POSS/PI composite fibers, we adopted XPS measurement to detect changes in chemical component and elemental states on the surface of composite fibers before and after AO exposure. Fig. 7 shows the XPS survey spectra of 10 wt% and 20 wt% POSS/PI composite fibers before and after AO exposure with an AO fluence of 2.93×10^{20} atoms cm^{-2}, and the elemental species and contents are presented in Table 5. Besides C1s and O1s peaks, small Si 2p and Si 2s peaks near 100 eV were observed before AO erosion in the XPS curve of composite fibers. After AO exposure, the contents of carbon atoms for 10 wt% and 20 wt% POSS/PI composite fibers decreased from 76.59% to 30.20% and from 74.72% to 26.15%, respectively. However, the contents of oxygen atoms for 10 wt% and 20 wt% POSS/PI composite fibers showed a clear increase from 18.63% to 45.19% and from 18.54% to 45.23%, respectively. Notably, the contents of silicon atom exhibited a dramatic growth from 3.81% to 22.78% and from 5.09% to 27.2%, for the 10 wt% and 20 wt% POSS/PI composite fibers. Actually, strong oxidizing AO can react with the atoms on fiber surfaces, such as carbon, hydrogen, nitrogen, and silicon. During the AO exposure process, some of these atoms were transformed to volatile gases, and the corresponding atom content was decreased

considerably. However, the formed silicon dioxide were nonvolatile; therefore, the oxygen and silicon contents rose dramatically on the surface [50]. Furthermore, the position and relative intensity of the peak at 101.9 eV assigning to Si−O changes obviously when the fibers were exposed to AO (Fig. 7b), which corresponds to a structural change from the $RSiO_{1.5}$ (POSS) at 101.9 eV to the high oxidation state of SiO_2 (103.3 eV). From the XPS results shown above, we confirmed that the surface-enriched POSS were transformed to the silica layer under the AO erosion and can cause the fibers to show excellent AO resistant character.

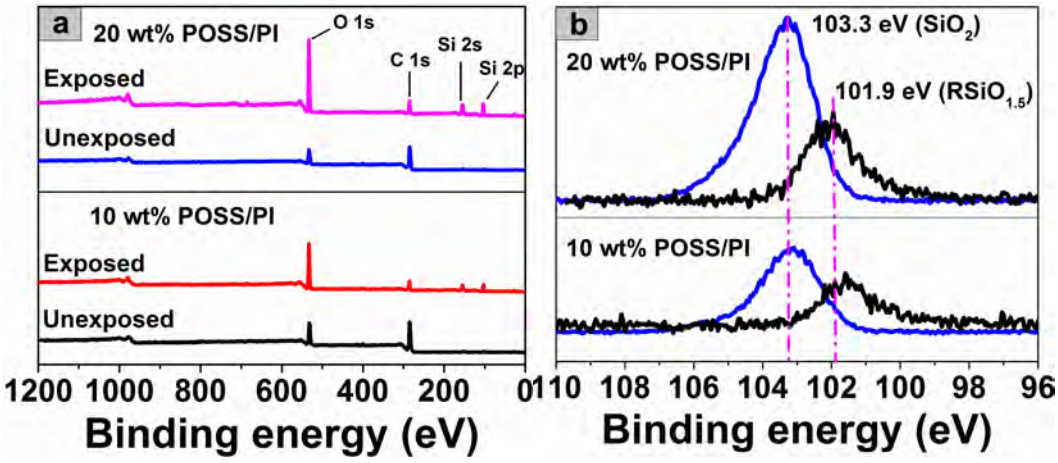

Fig. 7. (a) XPS survey spectra and (b) high resolution Si spectra of 10 wt% and 20 wt% POSS/PI composite fibers before and after AO exposure.

Table 5. Surface composition of the POSS/PI composite fibers before and after AO exposure.

Type of element	Elemental content (%)			
	10 wt% POSS/PI		20 wt% POSS/PI	
	Unexposed	Exposed	Unexposed	Exposed
C	76.59	30.20	74.72	26.15
O	18.63	45.19	18.54	45.23
Si	3.81	22.78	5.09	27.20

3.7. Mechanical Properties of Fibers after AO Erosion

Decrease in mechanical performance caused by AO erosion is a main problem to be solved for the high-performance fibers applied in LEO at present[4,52]. Consequently, the mechanical properties of POSS/PI composite fibers before and after AO exposure are shown in Fig. 8. The fracture strength and initial modulus of pristine PI fiber almost linearly decreased with a constant decay rate with increased AO fluence from 0 atoms cm^{-2} to 2.93×10^{20} atoms cm^{-2}, and the values rapidly decreased from 0.59 GPa to 0.32 GPa and from 7.41 GPa to 4.73 GPa. Such substantial decrease in mechanical properties of the fibers under AO exposure was fatal to the spacecraft in LEO. By contrast, under the same AO erosion conditions, the changes in mechanical properties of the POSS/PI fibers were remarkably lower. With increased AO fluence from 0 atom cm^{-2} to 2.93×10^{20} atoms cm^{-2}, the fracture strengths of the composite fibers with POSS contents of 5 wt%, 10 wt%, 15 wt%, and 20 wt% showed decreases from 0.59 GPa to 0.38 GPa, 0.61 GPa to 0.52 GPa, 0.56 GPa to 0.50 GPa, and 0.45 GPa to 0.42 GPa, respectively. For the initial modulus of the composite fibers with POSS contents of 5 wt%, 10 wt%, 15 wt%, and 20 wt%, the values declined from 7.37 GPa to 5.15 GPa, 7.58 GPa to 6.89 GPa, 7.22 GPa to 6.12 GPa, and 6.78 GPa to 6.20 GPa with increased AO fluence from 0 atom cm^{-2} to 2.93×10^{20} atoms cm^{-2}. Definitely, the retention of fracture strength and initial modulus of the fibers increased from 54% to 93% and 64% to 91% with increased POSS contents from 0

wt% to 20 wt%. Notably, although the pristine fracture strengths of the 15 wt% POSS/PI and 20 wt% POSS/PI composite fibers were slightly lower than that of pristine PI fiber, the retentions of fracture strength and initial modulus of the two samples were obviously higher than that of the pristine PI fiber after AO exposure. These results demonstrate that the AO resistance of the POSS/PI composite fibers improved considerably with increased POSS content. Thus, the improved AO resistance is likely sustainable even under increased AO fluence conditions; this notion implies that the service time of POSS/PI composite fibers applied in LEO can be effectively extended [50].

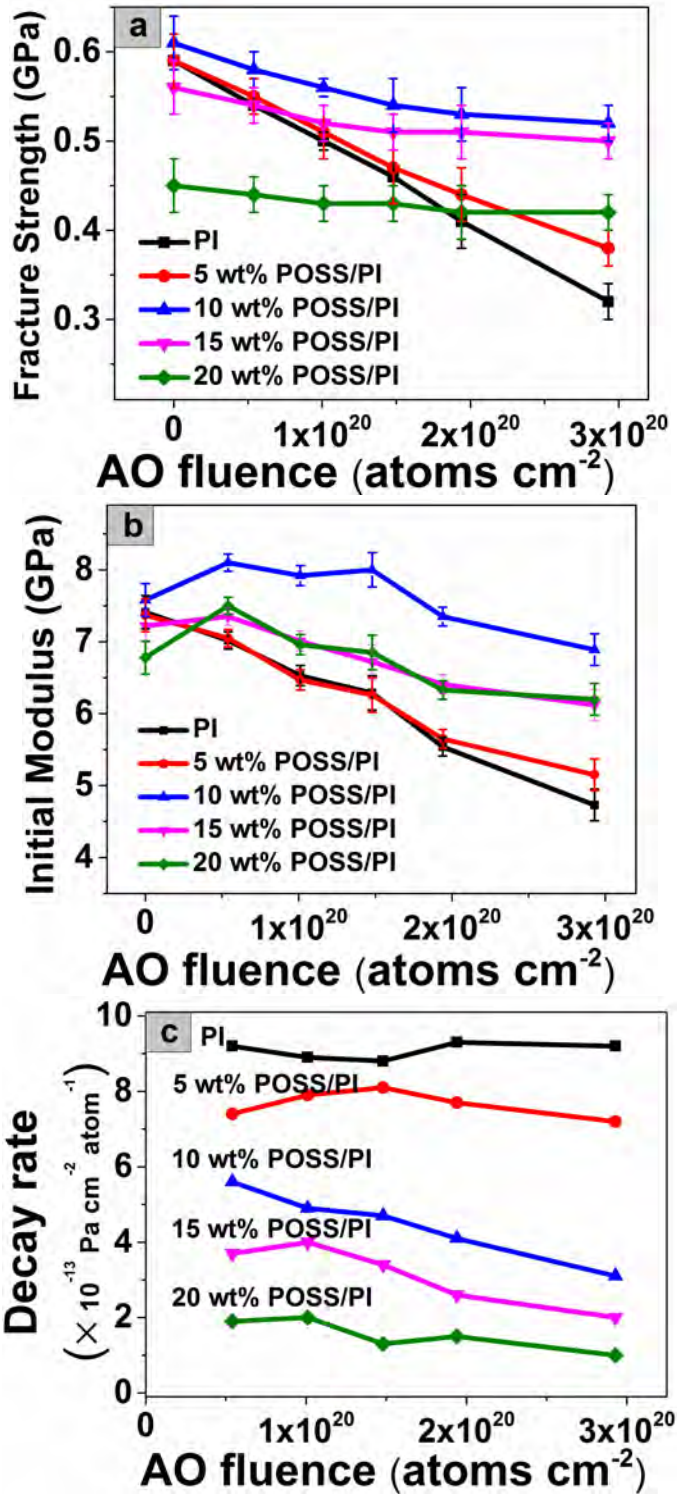

Fig. 8. Variation in (a) fracture strength, (b) initial modulus, and (c) fracture strength decay rate of POSS/PI composite fibers with AO fluences.

To quantitatively investigate the AO resistance of these fibers, the decay rate of mechanical performance of fibers was adopted as a relevant parameter for evaluating and comparing the AO resistance of the fiber materials. The fracture strength decay rate was defined in Equation (2) as follows:

$$D = (S_O - S)/F \quad (2)$$

where D is the fracture strength decay rate (Pa cm^2 atom^{-1}), So denotes the pristine value of fracture strength (Pa) before AO irradiance, S represents the retention value of fracture strength (Pa) after AO irradiance, and F is the AO fluence (atom cm^{-2}). The decay rate of these fibers is calculated, and the detailed results are shown in Fig. 8(c). The strength decay rate of PI fiber was found to be similar under the different AO fluences, with an average decay rate of 9.1×10^{-13} Pa cm^2 atom^{-1}. The strength decay rates of the POSS/PI composite fibers revealed a dramatic decrease from 9.2×10^{-13} Pa cm^2 atom^{-1} to 1.9×10^{-13} Pa cm^2 atom^{-1}, 8.9×10^{-13} Pa cm^2 atom^{-1} to 2.0×10^{-13} Pa cm^2 atom^{-1}, 8.8×10^{-13} Pa cm^2 atom^{-1} to 1.3×10^{-13} Pa cm^2 atom^{-1}, 9.3×10^{-13} Pa cm^2 atom^{-1} to 1.5×10^{-13} Pa cm^2 atom^{-1}, and 9.2×10^{-13} Pa cm^2 atom^{-1} to 1.0×10^{-13} Pa cm^2 atom^{-1} with increased POSS content from 0 wt% to 20 wt% with AO exposure at 5.4×10^{19}, 1.01×10^{20}, 1.48×10^{20}, 1.94×10^{20}, and 2.93×10^{20} atoms cm^{-2}. Furthermore, with increased AO fluences, the strength decay rates of the POSS/PI composite fibers presented a downward trend. The results indicate that the AO surface erosion exerted a gradually decreasing influence on the mechanical properties of the POSS/PI composite fibers with incremental POSS contents and AO fluences.

3.8. Relationship between Structure and AO Resistance Properties

For the POSS/PI fibers, the mass loss revealed a lower decrease than the mass loss of Kapton film and pristine PI fiber. With increased AO from 5.4×10^{19} atoms cm^{-2} to 2.93×10^{20} atoms cm^{-2}, the mass losses of 5 wt%, 10 wt%, 15 wt%, and 20 wt% POSS composite fibers exhibited a slow increase from 0.01 mg cm^{-2} to 0.04 mg cm^{-2}, 0.005 mg cm^{-2} to 0.035 mg cm^{-2}, 0.005 mg cm^{-2} to 0.020 mg cm^{-2}, and 0.005 mg cm^{-2} to 0.015 mg cm^{-2}, respectively.

Meanwhile, the surface morphologies of POSS/PI composite fibers showed an obvious improvement relative to that of pristine PI fiber after AO exposure experiment. When the POSS content was raised from 5 wt% to 15 wt%, the surface roughness of composite fibers clearly decreased after exposure at the same AO fluence, although the roughness of the fibers displayed increased with increased AO fluence from 0 atom cm^{-2} to 2.93×10^{20} atoms cm^{-2}. Notably, when the added POSS content reached 20 wt%, the surface roughness of composite fibers shows a slight change without obvious defect, although the AO fluence was increased to 2.93×10^{20} atoms cm^{-2}.

At the AO fluence of 2.93×10^{20} atoms cm^{-2}, the retention of fracture strength and initial modulus of the fibers showed an increase from 54% to 93% and 64% to 91% with increased POSS content from 0 wt% to 20 wt%. The strength decay rates of the POSS/PI composite fibers dramatically decreased from 1.9×10^{-13} Pa cm^2 atom^{-1} to 1×10^{-13} Pa cm^2 atom^{-1} at the AO fluence of 2.93×10^{20} atoms cm^{-2} with increased POSS content from 0 wt% to 20 wt%.

The mechanism of decreased mechanical performance of the fibers originated from the crack of the AO erosive fiber surface defects as observed from SEM [50]. Defect points, such as cracks or pits, in the fiber surface are expected to become initiation points of rupture. We assumed that when the fiber samples were loaded, stress concentrates at the defect region on rough surfaces produced by AO erosion, and then the defect region can develop a surface crack perpendicular to the loading direction [53]. The stress concentrated at the initial defect points reached a critical level, and the cracks began to grow and lead to failure. Therefore, a roughened surface can enlarge the stress concentration and reduce the rupture strength. As considered from fiber surface SEM analysis after AO exposure, the pristine PI fiber shows the roughest surface. As a consequence, the pristine PI fiber achieved the highest strength decay rate [54]. By contrast, the surface of POSS/PI composite fibers were smoother than that of PI fiber because of the formation of a dense surface layer of silica through the reaction of POSS and AO. Accordingly, the AO attack exerted a lower influence

than that of PI fiber on the mechanical performances of POSS/PI. Furthermore, given the increased content and surface enrichment of POSS, a continuous protective layer can be formed on the surfaces and effectively maintains the mechanical properties of POSS/PI composite fibers.

4. CONCLUSIONS

A series of POSS/PI composite fibers was initially prepared by in situ polymerization, followed by wet spinning and thermal imidization, with a POSS loading of 0 wt% to 20 wt%. The thermal and mechanical properties, and AO resistance performance of the POSS/PI composite fibers were subsequently investigated systematically. The main results are summarized as follows:

(i) With increased POSS content from 0 wt% to 20 wt%, the T_gs of POSS/PI fibers increase from 382 °C to 401 °C, and the $T_{5\%}$ was in the range of 560–570 °C, indicating good thermal properties for composite fibers.

(ii) After AO exposure with the fluence of 2.93×10^{20} atoms cm^{-2}, the mass loss of the composite films reveal an obvious decrease from 0.110 mg cm^{-2} to 0.015 mg cm^{-2}, with POSS content increasing from 0 wt% to 20 wt%; POSS/PI fibers display a compact surface, whereas the pure PI fiber possesses a loose surface; the retention of fracture strength and initial modulus is improved dramatically from 54% to 93% and 64% to 91%, respectively; the strength decay rate reveals a dramatic decrease from 1.9×10^{-13} Pa cm^2 $atom^{-1}$ to 1.0×10^{-13} Pa cm^2 $atom^{-1}$. Therefore, the composite fibers display excellent AO resistance even at higher fluence.

(iii) The quantitative analyses of the specific locations show that POSS nanoparticles enrich on the POSS/PI fiber surface. This effect is attributed to the kinetic competition between the POSS's outward diffusion and a gradual thickening of the outer gel layer in the dual diffusion process. Consequently, a thin silica layer forms easily on the fiber surface upon AO exposure, which can protect the fibers from further AO erosion.

These results show that the synthesized POSS/PI composite fibers possess excellent AO resistance performance and are highly promising for use as space materials.

AUTHOR INFORMATION

Corresponding Author

E-mail: xp_q@ciac.ac.cn; lxgao@ciac.ac.cn.

ACKNOWLEDGMENTS

This work was supported by the National Key R&D Program of China (2017YFB0308300). We also thank Beihang University for their help in ground-based simulated AO exposure experiment.

REFERENCES

[1] H.R. Fischer, K. Tempelaars, A. Kerpershoek, T. Dingemans, M. Iqbal, H. Lonkhuyzen, B. Iwanowsky, C. Semprimoschnig, Development of flexible LEO-resistant PI films for space applications using a self-healing mechanism by surface-directed phase separation of block copolymers. ACS Appl. Mater. Inter. 2 (2010) 2218-2225.

[2] P. Wang, Y. Tang, Z. Yu, J. Gu, J. Kong, Advanced Aromatic Polymers with Excellent Antiatomic Oxygen Performance Derived from Molecular Precursor Strategy and Copolymerization of Polyhedral Oligomeric Silsesquioxane. ACS Appl. Mater. Inter. 7 (2015) 20144-20155.

[3] L. Chen, Z. Li, C. Lee, J. Wang, Unified model for low-Earth-orbital atomic-oxygen and atomic-oxygen/ultraviolet induced erosion of polymeric materials. Aerosp. Sci. Technol. 53 (2016) 194-206.

[4] V.N. Chernik, L.S. Novikov, G.G. Bondarenko, A.I. Gaidar, T.N. Smirnova, Study of polymeric fiber erosion under oxygen plasma beams. Bull. Russ. Acad. Sci.: Phys. 74 (2010) 268-271.

[5] L. Ghosh, H. Kinoshita, N. Ohmae, Degradation on a mechanical property of high-modulus aramid fiber due to

hyperthermal atomic oxygen beam exposures. Compos. Sci. Technol.67 (2007) 1611-1616.

[6] L. Chen, C. Wang, Z. Wu, G. Wu, Y. Huang, Atomic oxygen erosion behaviors of PBO fibers and their composite: Microstructure, surface chemistry and physical properties. Polym. Degrad. Stab. 133 (2016) 275-282.

[7] X. Sui, L. Gao, P. Yin, Shielding Kevlar fibers from atomic oxygen erosion via layer-by-layer assembly of nanocomposites. Polym. Degrad. Stab.110 (2014) 23-26.

[8] L. Ghosh, M.H. Fadhilah, H. Kinoshita, N. Ohmae, Synergistic effect of hyperthermal atomic oxygen beam and vacuum ultraviolet radiation exposures on the mechanical degradation of high-modulus aramid fibers. Polymer 47 (2006) 6836-6842.

[9] F. Rahmani, S. Nouranian, X. Li, A. Al-Ostaz, Reactive Molecular Simulation of the Damage Mitigation Efficacy of POSS-, Graphene-, and Carbon Nanotube-Loaded Polyimide Coatings Exposed to Atomic Oxygen Bombardment. ACS Appl. Mater. Inter. 9 (2017) 12802-12811.

[10] Y. Huang, S. Lv, X. Tian, R.K.Y. Fu, P.K. Chu, Interface analysis of inorganic films on polyimide with atomic oxygen exposure. Surf. Coat. Technol. 216 (2013) 121-126.

[11] R. Cooper, H.P. Upadhyaya, T.K. Minton, M.R. Berman, X. Du, S.M. George, Protection of polymer from atomic-oxygen erosion using Al_2O_3 atomic layer deposition coatings. Thin Solid Films 516 (2008) 4036-4039.

[12] M. Shu, Z. Li, Y. Man, K. Liu, H. Liu, Y. Gao, Surface modification of poly (4,4'-oxydiphenylene pyromellitimide) (Kapton) by alkali solution and its applications to atomic oxygen protective coating. Corros. Sci. 112 (2016) 418-425.

[13] K. Liu, H. Mu, M. Shu, Z. Li, Y. Gao, Improved adhesion between SnO_2/SiO_2 coating and polyimide film and its applications to atomic oxygen protection. Colloids Surf. A 529 (2017) 356-362.

[14] H. Qi, Y. Qian, J. Xu, M. Li, Studies on atomic oxygen erosion resistance of deposited Mg-alloy coating on Kapton. Corrosion Science 124 (2017) 56-62.

[15] E. Ayandele, B. Sarkar, P. Alexandridis, Polyhedral Oligomeric Silsesquioxane (POSS)-Containing Polymer Nanocomposites. Nanomaterials 2 (2012) 445-475.

[16] T.K. Minton, M.E. Wright, S.J. Tomczak, S.A. Marquez, L. Shen, A.L. Brunsvold, R. Cooper, J. Zhang, V. Vij, A.J. Guenthner, B.J. Petteys, Atomic oxygen effects on POSS polyimides in low earth orbit. ACS Appl. Mater. Inter. 4 (2012) 492-502.

[17] M. Qian, V.J. Murray, W. Wei, B.C. Marshall, T.K. Minton, Resistance of POSS Polyimide Blends to Hyperthermal Atomic Oxygen Attack. ACS Appl. Mater. Inter. 8 (2016) 33982-33992.

[18] D. Peng, W. Qin, X. Wu, Improvement of the atomic oxygen resistance of carbon fiber-reinforced cyanate ester composites modified by POSS-graphene-TiO_2. Polym. Degrad. Stab. 133 (2016) 211-218.

[19] X. Li, A. Al-Ostaz, M. Jaradat, F. Rahmani, S. Nouranian, G. Rushing, A. Manasrah, H. Alkhateb, M. Finckenor, J. Lichtenhan, Substantially enhanced durability of polyhedral oligomeric silsequioxane-polyimide nanocomposites against atomic oxygen erosion. Eur. Polym. J. 92 (2017) 233-249.

[20] X. Lei, M. Qiao, L. Tian, P. Yao, Y. Ma, H. Zhang, Q. Zhang, Improved space survivability of polyhedral oligomeric silsesquioxane (POSS) polyimides fabricated via novel POSS-diamine. Corros. Sci. 90 (2015) 223-238.

[21] R. Misra, B.X. Fu, S.E. Morgan, Surface energetics, dispersion, and nanotribomechanical behavior of POSS/PP hybrid nanocomposites. J. Polym. Sci. Part B-Polym. Phys. 45 (2007) 2441-2455.

[22] R. Verker, E. Grossman, N. Eliaz, Effect of the POSS-Polyimide nanostructure on its mechanical and electrical properties. Compos. Sci. Tech. 72 (2012) 1408-1415.

[23] C. Teng, Y. Sheng, H. Tsao, Particle size-induced transition between surface segregation and bulk aggregation in a thin film of athermal polymer-nanoparticle blends. J. Chem. Phys. 146 (2017), 014904.

[24] J. Seyfi, I. Hejazi, S.H. Jafari, H.A. Khonakdar, F. Simon, Enhanced hydrophobicity of polyurethane via non-solvent induced surface aggregation of silica nanoparticles. J. Colloid Interface Sci. 478 (2016) 117-126.

[25] N. Hosaka, H. Otsuka, M. Hino, A. Takahara, Control of dispersion state of silsesquioxane nanofillers for stabilization of polystyrene thin films. Langmuir 24 (2008) 5766-5772.

[26] [26] R. Verker, E. Grossman, I. Gouzman, N. Eliaz, TriSilanolPhenyl POSS-polyimide nanocomposites: Structure-properties relationship. Compos. Sci. Tech. 69 (2009) 2178-2184.

[27] H. Lin, S. Kuo, C. Huang, F. Chang, Thermal and surface properties of phenolic nanocomposites containing octaphenol polyhedral oligomeric silsesquioxane. Macromol. Rapid Commun. 27 (2006) 537-541.

[28] R. Misra, B. Fu, A. Plagge, S.E. Morgan, POSS-Nylon 6 Nanocomposites: Influence of POSS Structure on Surface and Bulk Properties. J. Polym. Sci. Part B-Polym. Phys. 47 (2009) 1088-1102.

[29] R. Misra, A.H. Alidedeoglu, W.L. Jarrett, S.E. Morgan, Molecular miscibility and chain dynamics in POSS/polystyrene blends: Control of POSS preferential dispersion states. Polymer 50 (2009) 2906-2918.

[30] H.W. Milliman, M. Sanchez-Soto, A. Arostegui, D.A. Schiraldi, Structure-property evaluation of trisilanolphenyl POSS (R)/polysulfone composites as a guide to POSS melt blending. J. Appl. Polym. Sci. 125 (2012) 2914-2919.

[31] Y. Han, J. Wang, H. Zhang, Effects of kinetics coefficients on ternary phase separation during the wet spinning process. J. Appl. Polym. Sci. 125 (2012) 3630-3637.

[32] Q. Gao, H. Ma, W. Bao, C. Gao, M. Ge, Polyacrylonitrile/electroconductive TiO_2 nanoparticles composite fibers via wet-spinning. Fibers Polym. 17 (2016) 1048-1054.

[33] C. Yang, J. Dong, Y. Fang, L. Ma, X. Zhao, Q. Zhang, Novel Low-κ Polyimide Fibers with Simultaneously Excellent Mechanical Properties, UV-resistance and Surface Activity by Chemically Bonded Hyperbranched Polysiloxane, J. Mater. Chem. C 6 (2018) 1229-1238.

[34] J. Dong, C. Yin, X. Zhao, Y. Li, Q. Zhang, High strength polyimide fibers with functionalized graphene, Polymer 54 (2013) 6415-6424.

[35] E. Han, Y. Wang, X. Chen, G. Shang, W. Yu, H. Niu, S. Qi, D. Wu, R. Jin, Consecutive Large-Scale Fabrication of Surface-Silvered Polyimide Fibers via an Integrated Direct Ion-Exchange Self-Metallization Strategy, ACS Appl. Mater. Inter. 5 (2013) 4293−4301.

[36] H. Niu, M. Huang, S. Qi, E. Han, G. Tian, X. Wang, D. Wu, High-performance copolyimide fibers containing quinazolinone moiety: Preparation, structure and properties, Polymer 54 (2013) 1700-1708.

[37] W. Yang, F. Liu, J. Zhang, E. Zhang, X. Qiu, X. Ji, Influence of thermal treatment on the structure and mechanical properties of one aromatic BPDA-PDA polyimide fiber, Eur. Polym. J. 96 (2017) 429-442.

[38] W. Yang, F. Liu, G. Li, E. Zhang, Y. Xue, Z. Dong, X. Qiu, X. Ji, Comparison of different methods for determining the imidization degree of polyimide fibers, Chin. J. Polym. Sci. 34 (2016) 209-220.

[39] Y. Zhao, T. Feng, G. Li, F. Liu, X. Dai, Z. Dong, X. Qiu, Synthesis and properties of novel polyimide fibers containing phosphorus groups in the main chain. RSC Adv. 6 (2016) 42482-42494.

[40] Y. Zhao, Z. X. Dong, G. M. Li, X. M. Dai, F. F. Liu, X. Ma, X. Qiu, Atomic oxygen resistance of polyimide fibers with phosphorus-containing side chains, RSC Adv. 7 (2017) 5437-5444.

[41] Y. Zhao, G. Li, F. Liu, X. Dai, Z. Dong, X. Qiu, Synthesis and Properties of Novel Polyimide Fibers Containing Phosphorus Groups in the Side Chain (DATPPO), Chin. J. Polym. Sci. 35 (2017) 372-385.

[42] Y. Zhao, G. Li, X. Dai, F. Liu, Z. Dong, X. Qiu, AO-resistant properties of polyimide fibers containing phosphorous groups in main chains, Chin. J. Polym. Sci. 34 (2016) 1469-1478.

[43] Y. Zhao, Z. Dong, G. Li, X. Dai, F. Liu, X. Ma, X. Qiu, Atomic oxygen resistance of polyimide fibers with phosphorus-containing side chains. RSC Adv. 7 (2017) 5437-5444.

[44] E. Miyazaki, M. Tagawa, K. Yokota, R. Yokota, Y. Kimoto, J. Ishizawa, Investigation into tolerance of polysiloxane-block-polyimide film against atomic oxygen. Acta Astronaut. 66 (2010) 922-928.

[45] H. Shimamura, T. Nakamura, Mechanical properties degradation of polyimide films irradiated by atomic oxygen. Polym. Degrad. Stab. 94 (2009) 1389-1396.

[46] Y. Zhao, G. Li, X. Dai, F. Liu, Z. Dong, X. Qiu, AO-resistant properties of polyimide fibers containing phosphorous groups in main chains. Chin. J. Polym. Sci. 34 (2016) 1469-1478.

[47] J.W. Kim, J.S. Lee, Influence of the Draw Ratio on the Mechanical Properties and Electrical Conductivity of Nanofilled Thermoplastic Polyurethane Fibers. Fibers Polym. 18 (2017) 81-87.

[48] R. Misra, A.H. Alidedeoglu, W.L. Jarrett, S.E. Morgan, Molecular miscibility and chain dynamics in POSS/polystyrene blends: control of POSS preferential dispersion states. Polymer. 50 (2009) 2906-2918.

[49] U. Karabiyik, R. Paul, M.C. Swift, S.K. Satija, A.R. Esker, Effects of POSS Nanoparticles on Glass Transition Temperatures of Ultrathin Poly(t-butyl acrylate) Films and Bulk Blends. J. Polym. Sci. Part B-Polym. Phys. 53 (2015) 175-182.

[50] R. Verker, E. Grossman, N. Eliaz, Erosion of POSS-polyimide films under hypervelocity impact and atomic oxygen: The role of mechanical properties at elevated temperatures. Acta Mater. 57 (2009) 1112-1119.

[51] K. Yokota, S. Abe, M. Tagawa, M. Iwata, E. Miyazaki, J. I. Ishizawa, Y. Kimoto, R. Yokota, Degradation Property of Commercially Available Si-containing Polyimide in Simulated Atomic Oxygen Environments for Low Earth Orbit. High Perform. Polym. 22 (2010) 237-251.

[52] H. Shimamura, T. Nakamura, Mechanical properties degradation of polyimide films irradiated by atomic oxygen. Polym. Degrad. Stab. 94 (2009) 1389-1396.

[53] R. Verker, E. Grossman, I. Gouzman, N. Eliaz, POSS-Polyimide Nanocomposite Films: Simulated Hypervelocity Space Debris and Atomic Oxygen Effects. High Perform. Polym. 20 (2008) 475-491.

[54] R. Verker, N. Atar, F. Quero, S.J. Eichhorn, E. Grossman, Tensile stress effect on the macromolecular orientation and erosion mechanism of an atomic oxygen irradiated polyimide. Polym. Degrad. Stab. 98 (2013) 997-1005.